Int. J. Heat Mass Transfer. Vol. 35, No. 4, pp. 967–979, 1992
Printed in Great Britain

0017–9310/92 $5.00+0.00

The unsteady development of a GTA weld pool

MICHAEL KANOUFF
Sandia National Laboratories, Livermore, CA 94550, U.S.A.

and

RALPH GREIF
University of California, Berkeley, CA 94720, U.S.A.

(*Received* 10 *April* 1990 *and in final form* 19 *March* 1991)

Abstract—The governing equations for momentum, energy and electric transport are solved numerically to obtain the unsteady development of an axially symmetric gas tungsten arc weld pool. The effects of Marangoni, Lorentz and buoyancy forces are included. The finite difference method is used to solve the equations and the grid is made to adapt to the shape of the melt front and to move with the front as melting occurs. In general, convection is found to decrease the energy losses from the weld pool by evaporation. This increases the size of the weld pool. Convection has a large effect on the depth of the weld pool but only a small effect on the width. The Lorentz force causes fluid motions which increase the depth of the weld pool. The effects of the Marangoni force depend on the sign of the surface tension temperature coefficient, γ_T. A negative value for γ_T causes fluid motions which suppress the effects of the Lorentz force and result in a fairly shallow weld pool. A positive value for γ_T causes fluid motions which enhance the effects of the Lorentz force and result in a very deep weld pool.

1. INTRODUCTION

GAS TUNGSTEN arc welding (GTAW) is a form of fusion welding where an electric arc is applied to the surfaces of parts to be joined by melting and solidification. The arc transfers both energy and electrical current to the medium. The mechanisms which affect the shape of the time-dependent molten metal (weld pool) are the focus of this study. Most of the energy transferred from the arc is deposited on the surface of the metal. Energy losses from the surface occur mainly by radiation and evaporation [1]. Heat transfer within the weld pool occurs by both convection and conduction. The fluid motion is caused by forces resulting from buoyancy, electromagnetism and surface tension. Buoyancy results from the large temperature gradients created in the pool by the arc heating. The electromagnetic or Lorentz force results from the interaction of the electric current in the pool with the magnetic field induced by this current. The surface tension gradient on the weld pool free surface results from the gradient of the temperature at the surface. The objective of this work is to study the heat transfer and fluid motion in a GTA weld pool and, in particular, the influence that convection has on the time-dependent shape of the weld pool.

2. MODELING STUDIES

Rosenthal [2] used moving point and line heat sources to simulate an arc traveling over a semi-infinite medium. Comparisons with experimental results for fusion zone shapes and temperatures were generally poor due to the neglect of the finite arc heat flux distribution and convection in the weld pool [3, 4]. Distributed heat fluxes have been used by Pavlik *et al.* [5], Friedman and Glickstein [6] and Mills [7]. The neglect of weld pool convection, however, continued to result in poor agreement with experiment for weld shapes. Atthey [8] studied the effects of Lorentz forces on fluid flow in weld pools. He solved the Navier–Stokes equations for a weld pool with a constant hemispherical shape. The arc was simulated by an axially symmetric Gaussian current distribution.

Craine and Andrews [9] studied the effects of Lorentz forces on fluid motion and weld pool shapes in stainless steel. They solved the momentum and energy equations using the finite difference method with a body fitted grid to obtain steady axially symmetric shapes of the molten pool. Their results showed that fluid motion due to the Lorentz force has a pronounced effect on the shape of the pool. A single vortex was obtained with flow downward along the axis of symmetry, which increased the depth of the pool.

Oreper and Szekely [10] used finite differences to solve the governing equations for energy and momentum transport in GTA weld pools to determine the shape of the melt front. They included the effects of buoyancy, Lorentz and Marangoni forces (the Marangoni force is due to a gradient in the surface tension). Later, Oreper and Szekely [11] studied the formation of weld pools in aluminum, stainless steel and titanium. They found convection to be more important in poor conductors (titanium and stainless steel) than in a good conductor (aluminum). The

NOMENCLATURE

$\mathbf{A}_i$	area vector of control volume face i
$\mathbf{B}$	magnetic field vector
B_R	scale for the magnetic field, $\mu_0 I r_q/(2\pi r_e^2)$
c_p	specific heat
Ca	capillary number, $\mu V_R/\gamma$
D_p, R_p	pool depth at the axis of symmetry and radius at the surface, respectively
$\mathbf{e}_\theta$	unit vector in the cylindrical coordinate angular direction
Gr	Grashof number, $g\beta R^3 \Delta T_R/\nu^2$
h	enthalpy
H	height of domain
I	arc current
$\mathbf{J}$	electric current density vector
Jl	Joule number, $2\mu_0 \rho c_p \Delta T_R/B_R^2$
k	thermal conductivity
L	radius of domain
L_{fs}	heat of fusion
L_{fg}	heat of vaporization
n	distance measured normal to surface
Nu	$qR_p/\Delta T_R k_R$, where q is the local heat flux
p	pressure
P	total arc power
Pe	Peclet number, $\rho c_p R_p V_R/k$
R_1, R_2	orthogonal radii of curvature
r	radial coordinate
r_e	width of electrical flux distribution
r_q	width of thermal flux distribution
Re	Reynolds number, $R\rho V_R/\mu$
Rm	magnetic Reynolds number, $V_R \mu_0 R\sigma$
S	magnetic force number, $B_R^2/(\rho V_R^2 \mu_0)$
St	Stefan number, $c_p(T_f - T_0)/L_{fs}$
t	time, distance measured at a tangent to surface
T_f	fusion temperature
u, v	radial and axial velocity components, respectively
$\mathbf{V}$	velocity
Y	rate of mass vaporization
z	axial coordinate.

Greek symbols

γ	surface tension
γ_T	rate of change of surface tension with temperature
ε	position vector of interface, emissivity
μ	dynamic viscosity
μ_0	permeability of vacuum
ξ, η	transformed coordinates
σ	electrical conductivity, Stefan–Boltzmann constant
τ	shear stress.

Subscripts and superscripts

l, s	liquid and solid sides of interface, respectively
n	normal component
R	reference quantity
t	tangential component
∞	arc plasma
*	nondimensional quantities.

effect of convection was also found to be more important in deep weld pools than in shallow pools. Marangoni forces were found to have a strong effect on the circulation patterns.

Kou and Sun [12] calculated weld pool shapes for aluminum where the effects of buoyancy, Lorentz and Marangoni forces were included separately. Their results indicated that the Marangoni force was the most important source of fluid motion. Their results did not show a wide range of weld shapes. Kou and Wang [13] solved the governing three-dimensional equations for the case of a weld pool with a steady travel speed. Their results, however, were computed on a $26 \times 12 \times 13$ grid, which was probably too coarse to resolve the flow field in the pool.

Chan *et al.* [14] considered fluid motion in a two-dimensional traveling laser weld pool, where heat and momentum transfer in the direction of travel were neglected. They considered a range of parameter values representative of aluminum, stainless steel and sodium nitrate. Their results showed that the aspect ratio (width/depth) of the pool first increased with the absolute value of γ_T (only negative values of γ_T were considered) due to the radially outward flow caused by the Marangoni force. For larger values of $|\gamma_T|$, a secondary, counter rotating vortex formed which then resulted in a decrease of the aspect ratio with increasing $|\gamma_T|$.

Fautrelle [15] included convection in calculations of stationary weld shapes and found that the Lorentz and Marangoni forces dominated in causing fluid motion. His results clearly showed the difficulty in resolving the flow field near the melt front with a rectangular finite difference grid. Zacharia *et al.* [16] solved the governing three-dimensional equations for a traveling weld pool in aluminum where the free surface was not constrained to be flat. They showed only one weld shape and appeared to use a coarse grid.

Ramanan and Korpela [17] calculated steady weld pool shapes using a finite difference grid which had a large number of grid points and small grid point spacing. They noted that most of the previous studies used finite difference grids which did not resolve the thin momentum boundary layer.

It is difficult to compare the results from the differ-

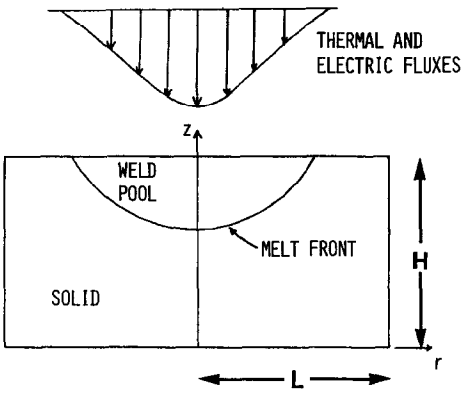

FIG. 1. A schematic showing the geometry of the problem to be solved.

ent investigators due to the different values of the parameters used. This may explain the large variations which exist between the computed weld shapes reported by different investigators. In general, the depth of the weld pool was shown to strongly depend on the convective heat transfer while the pool width was shown to be rather insensitive to the convective heat transfer. Chan *et al.* [14], however, showed that the pool width strongly depended on the convective heat transfer.

In the present work, axially symmetric weld pool shapes were studied. The process efficiency was not specified; rather an evaporation model was used to account for energy losses from the weld pool surface which yields an estimate of the process efficiency. The process efficiency, i.e. the net energy transferred from the arc to the medium divided by the total energy expended in the arc, was specified in the previous studies. A moving finite difference grid was used in this work. Conventional grids are not very efficient because of the moving and complex shape of the phase boundary. The method used here makes efficient use of the grid points by making the grid conform to the shape of the melt front.

The problem studied here, depicted in Fig. 1, is the formation of a spot weld using GTAW. A stationary arc is incident on a solid cylinder of diameter $2L$ and height H that is at a uniform temperature. The material is assumed to undergo a solid to liquid phase change at a single temperature. The current density and the heat flux distributions on the upper surface of the medium are specified boundary conditions using Gaussian distributions which fit experimental data [18]. Energy losses by radiation and metal vaporization are included. The finite difference method is used to solve Maxwell's equations and the governing equations for unsteady mass, momentum and energy transport. The equations are transformed to allow the use of a non-orthogonal moving finite difference grid.

3. FORMULATION OF THE BASIC EQUATIONS

The conservation equations are scaled using the width of the thermal flux distribution, r_q, for length, the quantities $\mu V_R/r_q$ for pressure, $c_{pR}\Delta T_R$ for enthalpy and r_q/V_R for time. In addition, density, thermal conductivity, specific heat and viscosity are scaled with the representative values, ρ_R, k_R, c_{pR} and μ_R, respectively. The reference scales for velocity and temperature are discussed below. The dimensionless equations are given by

$$\frac{D\rho^*}{Dt^*}+\rho^*\nabla^*\cdot\mathbf{V}^*=0 \tag{1}$$

$$\frac{\partial\mathbf{V}^*}{\partial t^*}+(\mathbf{V}^*\cdot\nabla^*)\mathbf{V}^*=-\frac{1}{Re\,\rho^*}\nabla^*P^*$$

$$+\frac{Gr}{Re^2\rho^*}(T^*-T_R^*)\mathbf{e}_z+2S(\mathbf{J}^*\times\mathbf{B}^*)$$

$$-\frac{2}{3Re\,\rho^*}\nabla^*(\mu^*\nabla^*\cdot\mathbf{V}^*)+\frac{\mu^*}{Re\,\rho^*}[\nabla^{*2}\mathbf{V}^*$$

$$+\nabla^*(\nabla^*\cdot\mathbf{V}^*)]+\frac{2}{Re\,\rho^*}(\nabla^*\mu^*\cdot\nabla^*)\mathbf{V}^*$$

$$+\frac{1}{Re\,\rho^*}\nabla^*\mu^*\times(\nabla^*\times\mathbf{V}^*) \tag{2}$$

$$\frac{\partial\rho^*h^*}{\partial t^*}+\nabla^*\cdot(\mathbf{V}^*\rho^*h^*)=\frac{8}{Rm\,Jl}\mathbf{E}^*\cdot\mathbf{J}^*$$

$$+\frac{1}{Pe}\nabla^*\cdot k^*\nabla^*T^*. \tag{3}$$

The buoyancy term in equation (2) has been linearized with respect to temperature.

Maxwell's equations govern the distribution of the current density, **J**, the electric field, **E**, and the magnetic field, **B**. These variables are scaled with the quantities I/r_e^2, $I/r_e^2\sigma$ and $I\mu_0 r_q/2\pi r_e^2$, respectively. Here, the electrical conductivity, σ, is assumed constant. For typical values of the parameters for welding applications, the magnetohydrodynamic (MHD) approximations may be used. In addition, the magnetic field is assumed to be steady and the free charge density is assumed to be zero. The resultant form of Maxwell's equations are [19]

$$\nabla^*\times\mathbf{E}^*=0,\quad 2\pi\nabla^*\times\mathbf{B}^*=\mathbf{J}^*. \tag{4}$$

Ohm's law, $\mathbf{J}^*=\mathbf{E}^*$, completes the set of three equations for the three unknowns, **E**, **J** and **B**.

The axially symmetric current density creates a magnetic field which is solely in the azimuthal direction. $\mathbf{B}^*$ is expressed in terms of Ψ^*, $\mathbf{B}^*=2\pi(\Psi^*/r^*)\mathbf{e}_\theta$, where Ψ^* was called an electromagnetic stream function by Oreper and Szekely [10]. The current density is expressed in terms of Ψ^* as

$$\mathbf{J}^*=\nabla^*\times\frac{\Psi^*}{r^*}\mathbf{e}_\theta \tag{5}$$

which yields

$$\frac{\partial}{\partial z^*}\left(\frac{1}{r^*}\frac{\partial \Psi^*}{\partial z^*}\right)+\frac{\partial}{\partial r^*}\left(\frac{1}{r^*}\frac{\partial \Psi^*}{\partial r^*}\right)=0. \quad (6)$$

3.1. *The boundary conditions*

(i) The upper surface is exposed to the electric and thermal fluxes from the arc. The heat flux entering the medium is equal to the incident arc flux minus the heat losses. Heat is lost from the upper surface primarily by radiation and vaporization. Thus

$$\Psi^* = \frac{3}{\pi}\int_0^{r^*} r^* \exp\left(\frac{-3r^{*2}}{r_e^{*2}}\right)dr^*$$

(z^* on the upper surface) (7)

$$k^*\frac{\partial T^*}{\partial z^*} = \frac{3P}{\pi r_q \Delta T_R k_R}[\exp(-3r^{*2}) - Y^*]$$

$$-\frac{r_q \Delta T_R^3 \varepsilon\sigma}{k_R}(T^{*4}-T_\infty^{*4}) \quad (z^* \text{ on the upper surface}) \quad (8)$$

where P, the total incident arc power, equals the product of the arc current, voltage and the factor 0.9; i.e. 10% is lost by direct radiation. Y, the rate of mass loss by evaporation, is calculated using the equation derived by Dushman and Lafferty based on kinetic theory (cf. Choi *et al.* [20]) which is of the form $\log Y = A - B/T - 1/2 \log T$, T being the local surface temperature in Kelvin. For stainless steel, with Y in g cm^{-2} s^{-1}, Choi *et al.* [20] recommend $A = 8.641$ and $B = 18\,732$. Y is scaled with $3P/(\pi r_q^2 L_{fg})$.

(ii) The temperature at the melt front is equal to the fusion temperature, T_f. The motion of the front is determined by the difference between the heat flux into the melt front on the liquid side and the heat flux away from the front on the solid side, cf. equation (9). Here, time is scaled by $r_q^2 c_{\rho R}\rho_R/k_R$, and ε is a position (or distance) vector which has a fixed but arbitrary reference point since only the change in ε is important

$$\frac{\rho^*}{St}\frac{d\varepsilon^*}{dt^*} = (k^*\nabla^* T^* \cdot \mathbf{n}^*)_l - (k^*\nabla^* T^* \cdot \mathbf{n}^*)_s$$

(r^*, z^* on the melt front). (9)

(iii) A symmetry condition exists at the axis, $r = 0$

$$\Psi^* = \frac{\partial T^*}{\partial r^*} = 0 \quad (r^* = 0). \quad (10)$$

(iv) The lower surface is insulated thermally and electrically

$$\Psi^* = \frac{\partial T^*}{\partial z^*} = 0 \quad (z^* = 0). \quad (11)$$

(v) The side surface is adiabatic. The current leaves the domain on the side surface with a uniform distribution

$$\frac{\partial T^*}{\partial r^*} = 0, \quad \Psi^* = \frac{r_e^{*2}}{2\pi H^*} z^* \quad (r^* = L^*). \quad (12)$$

(vi) The tangential and normal forces must balance at the free surface of the pool. The tangential forces result from the shear stress of the plasma above the surface, the shear stress of the liquid metal below the surface and the surface tension gradient on the free surface. The surface tension is approximated by the equation $\gamma = \gamma_R + \gamma_T(T - T_f)$, where γ_T is a constant, γ is scaled by $\gamma_T \Delta T_R$

$$\mu^*\left(\frac{\partial V_t^*}{\partial n^*}+\frac{\partial V_n^*}{\partial t^*}\right) = \mu_\infty^*\left(\frac{\partial V_t^*}{\partial n^*}+\frac{\partial V_n^*}{\partial t^*}\right)_\infty$$

$$\times \frac{\tau_\infty r_q}{\mu_R V_R \sqrt{(Re)}} + \frac{d\gamma^*}{dt^*} \quad (z^* \text{ on free surface}) \quad (13)$$

where n and t are the local normal and tangential coordinates to the free surface, the subscript ∞ signifies values corresponding to the arc plasma, δ is the thickness of the Marangoni shear layer discussed later and τ_∞ is the shear stress exerted on the weld pool free surface by the arc plasma. A representative value of τ_∞ is taken from the study of McKelliget and Szekely [21]. The normal forces on the free surface are the pressure of the plasma, the pressure in the liquid metal and the normal component of surface tension due to curvature

$$p^* - 2\left(\frac{\partial V_n^*}{\partial n^*}\right) - p_\infty^* \frac{p_\infty R_p}{\mu V_R} + 2\mu_\infty^*\left(\frac{\partial V_n^*}{\partial n^*}\right)_\infty \frac{\tau_\infty R_p}{\mu_R V_R}$$

$$= Ca^{-1}\left(\frac{1}{R_1^*}+\frac{1}{R_2^*}\right), \quad z^* \text{ on free surface.} \quad (14)$$

A representative value of p_∞ is taken from the study by Fan *et al.* [22].

(vii) The tangential fluid velocity is zero at the melt front and the normal fluid velocity depends on the change in density due to melting

$$V_t^* = 0, \quad V_n^* = \frac{d\varepsilon^*}{dt^*}\left(1-\frac{\rho_s}{\rho_l}\right)\frac{1}{Pe},$$

(r^*, z^*) on melt front. (15)

(vii) On the axis of symmetry the radial velocity and the radial gradient of the axial velocity are zero

$$\frac{\partial v^*}{\partial r^*} = u^* = 0 \quad (r^* = 0). \quad (16)$$

3.2. *The velocity and temperature scales*

The energy boundary condition, equation (8), leads to a relation for a temperature scale, ΔT_R, with dominant terms representing the vaporization heat loss and the incident arc heat flux. Equating these two terms gives the evaporation limiting temperature; subtracting T_f from the result gives ΔT_R; i.e. ΔT_R represents the temperature difference across the pool. Ostrach [23] derived the following velocity and thickness scales, V_R and δ, for a shear layer driven by Marangoni forces which are appropriate for this study. The Marangoni velocity scale is used in the

Table 1. Thermal physical properties and arc parameters

Properties of stainless steel (see Leibowitz [24] for the dependence of ρ, c_p and β on temperature)

$$\rho = 6.56 \text{ g cm}^{-3};\ c_p = 0.19 \text{ cal g}^{-1}\,^{\circ}\text{C}^{-1};\ T_f = 1400^{\circ}\text{C};\ L_{fs} = 65 \text{ cal g}^{-1};\ L_{fg} = 1754 \text{ cal g}^{-1};$$

$$k = 0.030 + 3.86 \times 10^{-5}\, T \text{ cal cm}^{-1}\text{ s}^{-1}\,^{\circ}\text{C}^{-1},\ T \leqslant T_f;\ k = 0.031 + 5.7 \times 10^{-6}\, T \text{ cal cm}^{-1}\text{ s}^{-1}\,^{\circ}\text{C}^{-1},\ T > T_f;$$

$$\mu = 0.01 \times 10^{(2385/T(\text{K}) - 0.5958)} \text{ g s}^{-1}\text{ cm}^{-1},\ T > T_f;\ \beta = 1 \times 10^{-4}\,^{\circ}\text{C}^{-1};\ \gamma_T = \pm 0.01 \text{ dyne cm}^{-1}\,^{\circ}\text{C}^{-1};$$

$$\sigma = 17894 - 6.5T\,\Omega^{-1}\text{ cm}^{-1},\ T \leqslant T_f;\ \sigma = 4976 - 1.2(T - T_f)\,\Omega^{-1}\text{ cm}^{-1},\ T > T_f$$

Arc parameters (typical values for a short arc length, e.g. 1 mm [18])

$$I = 100 \text{ A};\ V = 10.9 \text{ V};\ r_q = 0.356 \text{ cm};\ r_e = 0.326 \text{ cm};\ \eta = 0.9$$

evaluation of the dimensionless parameters. A velocity scale based on a balance between the Lorentz force and the inertial force, $V_{J\times B}$, is also noted (cf. Oreper and Szekely [11])

$$V_R = \left(\frac{\gamma_T^2 \Delta T_R^2}{r_q \rho_R \mu_R}\right)^{1/3},\quad \delta = \left(\frac{\mu_R^2 r_q^2}{\rho_R \gamma_T \Delta T_R}\right)^{1/3},$$

$$V_{J\times B} = \left(\frac{3\mu_0 r_q}{2H\rho_R}\right)^{1/2} \frac{ID_p}{\pi r_e^2}. \tag{17}$$

$V_{J\times B}$ has a linear dependence on the depth of the weld pool, D_p.

Based on the property values of stainless steel 304 [24] and the arc parameters [18] shown in Table 1, $\Delta T_R = 1049^{\circ}\text{C}$ and $V_R = 9.7 \text{ cm s}^{-1}$. The variation in density between room temperature and $\Delta T_R + T_f$ is 21%. Of this, 4% is due to melting, i.e. $\rho_s/\rho_l = 1.04$. The effect of this density variation on weld pools should be studied. However, to simplify the equations the density is held constant ($\rho = \rho_R = 6.56 \text{ g cm}^{-3}$, $\rho_s/\rho_l = 1$). An exception is made for the buoyancy term in the momentum equation where the density is assumed to be a linear function of temperature. The specific heat is taken to be a single constant value over the liquid and solid domains. The thermal expansion coefficient, β, is also taken to be constant. The variations of the thermal conductivity and the viscosity with temperature are included.

A total of 15 parameters are identified in the governing equations (Re, Gr, S, Pe and $Rm\,Jl$) and the boundary conditions (L^*, H^*, r_e^*, $P_\infty r_q/(\mu_R V_R)$, $\tau_\infty r_q/(\mu_R V_R)$, $P/(r_q \Delta T_R k_R)$, $r_q \Delta T_R^3 \varepsilon\sigma/k_R$, St, Ca and ρ_s/ρ_l (ρ_s/ρ_l was discussed above)). The value of the magnetic force number S is 0.49, indicating that the Lorentz force is of the same order of magnitude as the inertial force. The buoyancy force is smaller than the inertial force but not negligible ($Gr/Re^2 = 0.14$). The viscous force is much smaller than the inertial force in the bulk of the flow ($Re^{-1} = 0.0022$); however, the viscous force is dominant in the boundary layers near the weld pool free surface and also near the melt front. This can be demonstrated by rescaling the viscous term in the momentum equation using the boundary layer thickness scale. Heat transfer by convection is more important than by conduction in the bulk of the flow ($Pe^{-1} = 0.011$). Volumetric heating due to electrical power dissipation is small [$8/(Rm\ Jl) = 0.0021$] and is neglected (i.e. $Rm\ Jl^{-1}$ is set to zero). The energy associated with phase change is of the same order of magnitude as the change in sensible energy ($St = 3.1$).

From equation (8), $P/(r_q \Delta T_R k_R) = 13$ and $r_q \Delta T_R^3 \varepsilon\sigma/k_R = 0.01$, showing that the conduction term and the radiation terms are small in comparison to the arc heat flux and evaporation terms. Equation (13) contains the dimensionless grouping, $\tau_\infty r_q/(\mu V_R \sqrt{(Re)})$, equal to 0.25. This indicates that the shear stress on the free surface caused by the flow of the arc plasma is small, but not negligible. However, it is neglected in the interest of simplification; i.e. $\tau_\infty r_q/(\mu V_R \sqrt{(Re)})$ is set to zero. The deflection of the free surface depends on the values of [from equation (14)] the capillary number, Ca, and the dimensionless groupings $(p_\infty r_q/\mu_R V_R)$ and $(\tau_\infty r_q/\mu_R V_R)$. The latter two quantities have values of 30 and 5, respectively. The value of Ca is 4×10^{-4}, which indicates that the radius of curvature of the free surface is of the order of 100 cm. This rough analysis of the surface deflection indicates that surface deflections should be small so the free surface is assumed to be flat ($(p_\infty r_q/\mu_R V_R)$, $(\tau_\infty r_q/\mu_R V_R)$ and Ca are all set to zero). However, more detailed studies of surface deflections are warranted. The values of the remaining parameters are $L^* = H^* = 2.8$ and $r_e^* = 0.92$.

4. THE METHOD OF SOLUTION

Figure 2 shows a diagram of the moving grid used in this study with the melt front coinciding with $\eta = \eta_{melt}$ and the liquid domain defined by $\eta > \eta_{melt}$. Figure 3 shows the grid that was used. The grid points are distributed along straight lines of constant ξ extending from the upper left hand corner of the grid, through the melt front and over to either the lower or right hand boundaries. A predetermined grid point distribution along the straight lines is used, with a smaller grid point spacing near the melt front. The spacing of the lines of constant ξ is also predetermined. This spacing is made smaller near the free surface of the pool. The grid point movement is due solely to the movement of the melt front. The remainder of the grid is made to stretch with the motion of the melt front preserving the relative spacing discussed above. The lines of constant ξ do not move during the calculation. Most of the calculations are carried out using a moving grid which conforms to the shape of the weld pool. Prior to the occurrence of melting a stationary grid is used. During this small time interval

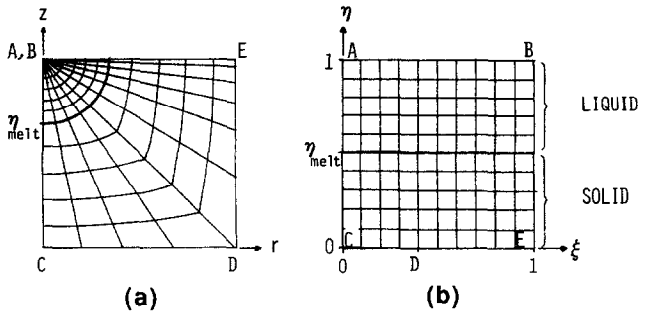

FIG. 2. A schematic of the finite difference grid as it appears in physical (a) and transformed space (b). The points labeled A–E in the (r,z) plane map into the corresponding points in the (ξ, η) plane.

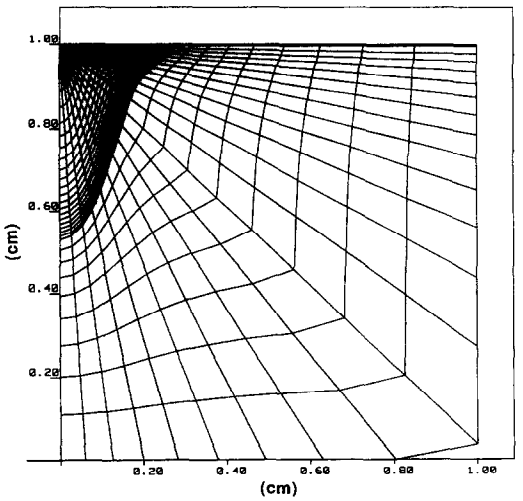

FIG. 3. The finite difference grid as it appeared at the end of the calculation for the $\gamma_T = 0.01$ dyne cm^{-1} °C^{-1} case.

the heat transfer is dominated by heat conduction. The conduction equation is solved using the apparent specific heat method to account for the heat of fusion. The calculation is stopped when the fusion temperature isotherm has propagated a small distance. A new grid is then constructed which conforms to the melt front and moves with it for the remainder of the calculation. It is on the moving grid that the equations of motion are solved to determine the flow field in the liquid domain for use in the advection terms in the energy transport equation. The amount of melting during the stationary grid calculation is restricted to be small.

A transformation from cylindrical coordinates to generalized moving curvilinear coordinates was accomplished by first writing the equations in control volume form. This was done for three reasons: one, only first order derivatives appear in these equations which are easily transformed with a single application of the chain rule; two, this approach leads directly to the conservative form of the transformed equations; and three, the arc heat flux can be included in the energy equation for control volumes surrounding boundary nodes. This yields a more accurate representation of the heat flux boundary condition than the conventional method which uses a temperature difference between two grid points perpendicular to the surface. A detailed discussion of the transformation may be found in Kanouff [25]. Central finite difference expressions are used to approximate the spatial derivatives. Time integration is accomplished using a predictor–corrector method similar to the alternating direction implicit (ADI) method. The stream function and electromagnetic stream function equations are solved directly using LDU decomposition. The energy balance at the melting front is solved explicitly.

A 41×26 grid size was used where the portion of the grid dedicated to the liquid domains was 32×26 and the portion of the grid dedicated to the solid domain was 9×26. In order to resolve the Marangoni shear layer, a minimum grid spacing of 0.0009 cm was used near the free surface. This small grid spacing required the use of a small time step in order to preserve stability. As a result, 24 h of CRAY YMP CPU time was required to calculate a weld pool corresponding to 10 s of arc time. A comprehensive convergence study was carried out [25]. For most cases the effects of changes in grid spacing, time step and convergence tolerances were found to be less than 1% for the velocities and temperatures. At the melt front a 3% effect was found on the Nusselt number near the surface for $\gamma_T = -0.01$ dyne cm^{-1} °C^{-1}. For the $\gamma_T = 0.01$ case, a 2% effect on the Nusselt number was found near the axis of symmetry for small time which grew to 10% for large time.

5. PRESENTATION AND DISCUSSION OF THE RESULTS

The results for the formation of axially symmetric weld pools are presented. The values of the parameters noted at the end of Section 2 were used. Note that the negative value of γ_T corresponds to a pure material whose surface tension has a maximum value at the fusion temperature and decreases monotonically to zero as the critical temperature is reached. The positive value corresponds to a material with impurities such as sulfur present. Sulfur concentrations as small as 50 p.p.m. cause the surface tension of iron to increase

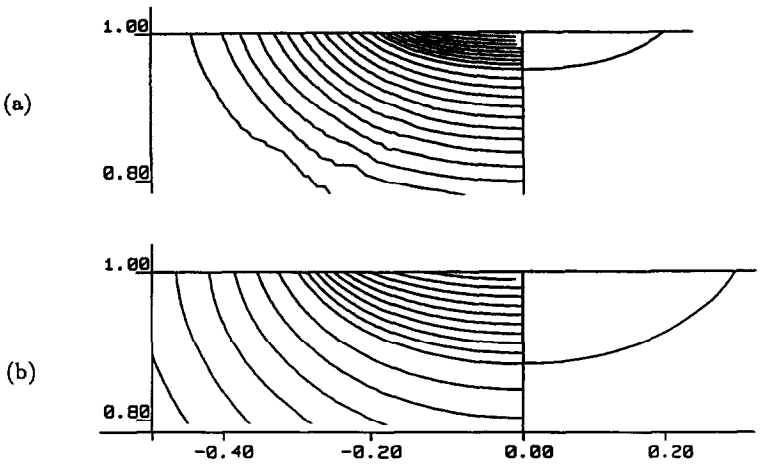

FIG. 4. The shape of the weld pool (right) and the temperature distribution (left, shown in 100°C contour intervals) in the vicinity of the pool for pure conduction: (a) $t = 0.25$ s; (b) $t = 10$ s.

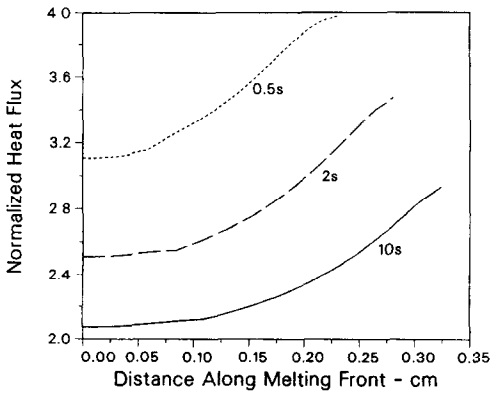

FIG. 5. Pure conduction results for the variation of the heat flux along the liquid side of the melt front normalized by $k_R \Delta T_R / R_p$, where R_p is the radius of the pool.

with temperature over a large temperature range [26, 27]. Heiple and Roper [28] showed that the depth to width ratio of welds increased dramatically due to small amounts of sulfur.

Figure 4(a) shows the shape of the weld pool and the temperature distribution obtained from the conduction formulation. The location of the melt front corresponding to $t = 0.25$ s (with arc initiation at $t = 0$ s) can be seen on the right side of Fig. 4(a). The subsequent calculations are all carried out with a moving grid tracking the melt front. To provide a comparison for the calculations including the effects of convection, a pure conduction calculation ($Pe = 0$) was carried out. Figure 4(b) shows the result from this conduction calculation for the weld shape and temperature field at a weld time of 10 s. Figure 5 shows the distribution of the heat flux along the liquid side of the melt front. The heat flux increases with distance measured along the melt front, starting from the bottom center of the pool, and decreases at all locations on the front with respect to time.

The following results are from calculations which included the effects of convection as determined from the full solution of the unsteady equations of motion for $\gamma_T = -0.01$ dyne cm^{-1} °C^{-1}. Figure 6 shows the stream function and temperature fields at 0.5, 2 and 10 s. The vortex on the right in Fig. 6(a), filling most of the pool, is driven by the Marangoni force. Surface tension, in this case, is larger at the colder pool perimeter than at the hot center of the free surface. The net force acts to pull the fluid on the free surface radially outward causing the vortex, shown in Fig. 6(a), to rotate in the clockwise direction. A counter clockwise rotating vortex driven by the Lorentz force is located near the axis, $r = 0$, although it is weak and does not appear in Fig. 6(a). As the weld pool gets wider with time the Marangoni vortex (next to the surface) moves out along the free surface staying near the pool perimeter. This permits the Lorentz vortex (next to the axis, $r = 0$) to increase in size and strength, although the Marangoni vortex appears to restrict the Lorentz vortex to the lower portion of the pool.

Figure 7 shows the radial component of velocity along the free surface at $t = 10$ s. The maximum velocity is located near the outer perimeter where the maximum surface tension gradient is located. Also shown in Fig. 7 is the axial component of velocity as a function of depth along the axis ($r = 0$). The velocity is initially quite small and remains much smaller than the radial component of velocity on the free surface.

The Nusselt number, Nu, along the melt front (liquid side) is shown in Fig. 8. At 0.5 s the Nu distribution appears similar to the conduction result (Fig. 5) except near the free surface. The maximum value of the Nusselt number is not located at the free surface; instead, it is located just below the surface. This is apparently due to the large outward radial velocities near this point which turn downward near the outer edge of the pool. Note that the value of Nu at the surface remains larger than the pure conduction

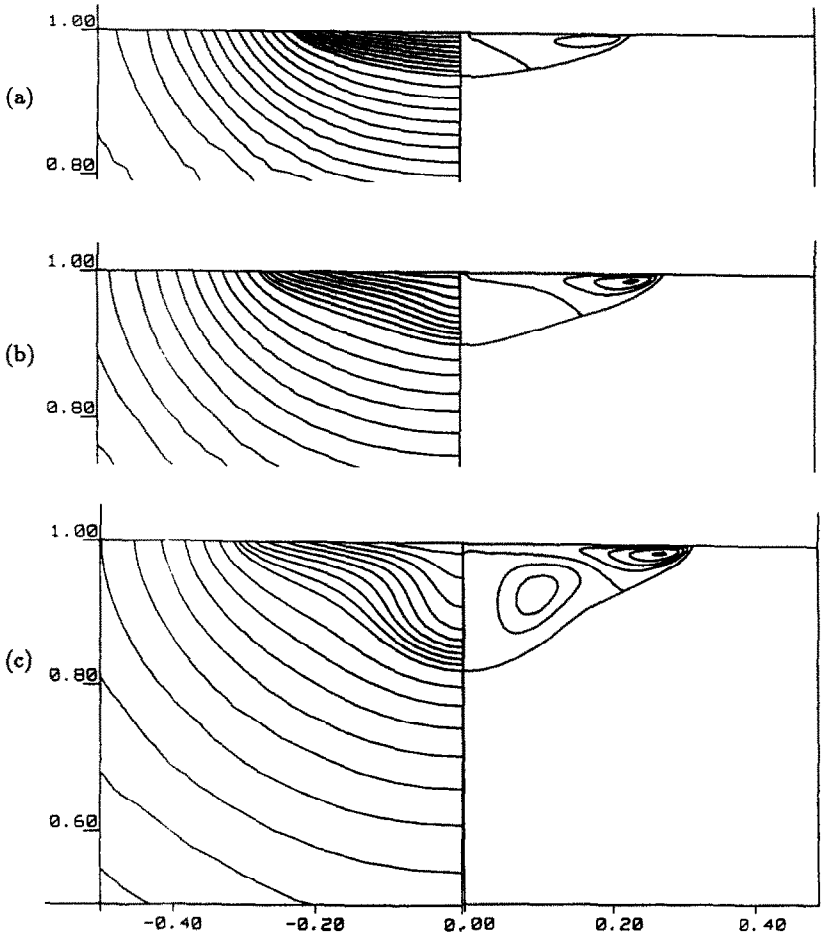

FIG. 6. The shape of the weld pool and the stream lines (right, shown in increments of 0.003 $cm^3 s^{-1}$) and the temperature distribution (left, shown in 100°C contour intervals) in the vicinity of the pool for $\gamma_T = -0.01$ dyne cm^{-1} $°C^{-1}$: (a) $t = 0.5$ s; (b) $t = 2$ s; (c) $t = 10$ s.

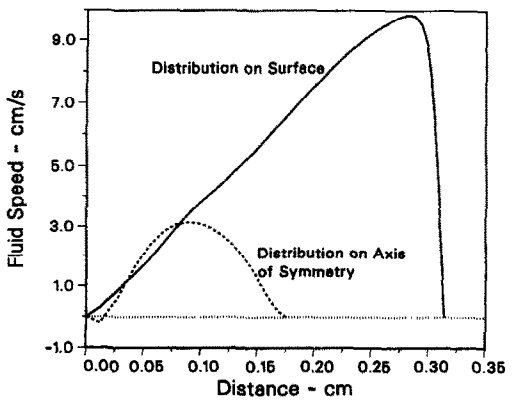

FIG. 7. The variations of the radial component of velocity along the free surface and the axial component of velocity along the axis of symmetry for the $\gamma_T = -0.01$ dyne cm^{-1} $°C^{-1}$ case.

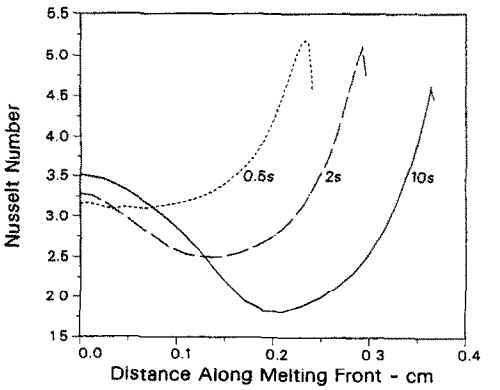

FIG. 8. The variation of the Nusselt number along the liquid side of the melt front for the $\gamma_T = -0.01$ dyne cm^{-1} $°C^{-1}$ case.

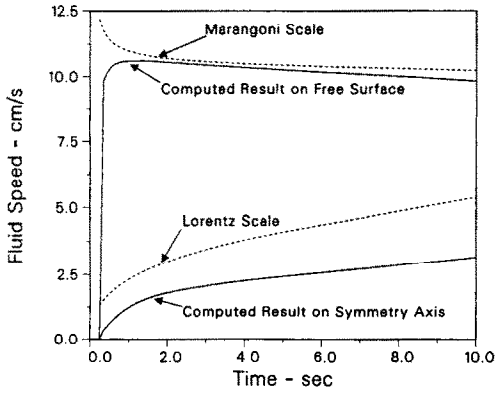

FIG. 9. The maximum fluid velocities on the free surface (radial component) and on the axis of symmetry (axial component) for the $\gamma_T = -0.01$ dyne cm^{-1} °C^{-1} case. The Marangoni and Lorentz velocity scales are shown for comparison.

result; that is, the effect of convection in this case is to increase *Nu* at all points on the melt front. As time progresses a local maximum develops at the axis due to the increasing strength of the Lorentz vortex.

The maximum values of the velocity on the free surface (radial component) and the axis (axial component), are shown in Fig. 9 as a function of time. Also shown are the Marangoni and Lorentz velocity scales (equations (17)) based on the temperature scale (evaporation limit) and on the computed, time-dependent values of the pool depth and radius [r_q in equations (17) is replaced with R_p, the radius of the pool at the surface]. The correlation between the computed results and the scales is good. The magnitude of the Marangoni velocity scale is close to the maximum velocity on the surface and both the scale and the computed result decrease as the width of the pool increases. Although the magnitude of the Lorentz scale is approximately twice the value of the maximum velocity on the axis of symmetry, the computed result is approximately linear with the depth of the pool, as predicted by the Lorentz scale. The good correlation shown in Fig. 9 indicates that the unsteady term in the momentum equation is small (except for small time) since there is no time dependence in equations (17). Thus, the flow field is quasi-steady, i.e. a function of weld shape only. Figure 9 shows that the velocity quickly attains the quasi-steady value (<0.1 s).

Calculations were also carried out for a positive value of γ_T, 0.01 dyne cm^{-1} °C^{-1} (cf. Fig. 10). In this case the Marangoni force drives the free surface fluid radially inward. Recall that the Lorentz force also drives fluid near the free surface radially inward. Thus, both forces drive a single strong and deep vortex rotating in the counter clockwise direction in Fig. 10, which convects heat downward along the axis, $r = 0$. This results in a large heat flux at the bottom of the weld pool (cf. Fig. 12) and a deep weld pool results.

Figure 11 shows the inward (negative) radial velocity distribution along the free surface and the axial velocity distribution along the axis, $r = 0$, at $t = 10$ s. The velocities are much larger than for the $\gamma_T = -0.01$ case due to the downward influx of momentum from both the Marangoni and Lorentz forces. (For $\gamma_T = -0.01$ the Marangoni and Lorentz forces oppose one another which results in two separate, weaker vortices.) In contrast to the $\gamma_T = -0.01$ case, the velocity distribution is not symmetrical; rather, the maximum value is located near the free surface.

The Nusselt number distribution along the melt front, shown in Fig. 12, has a maximum value at the axis of symmetry due to the strong downward convection at $r = 0$. Figure 13 shows the maximum velocities on the free surface and along the axis, $r = 0$. The characteristic velocity scales given by equations (17) (with r_q replaced by R_p, the radius of the pool at the surface) are also shown. The maximum computed velocities are nearly equal and are also much larger than the two respective scales. This is because the scalings from the Marangoni and Lorentz forces are for independent and separate vortices.

The variation of pool depth as a function of time is shown in Fig. 14(a) for the pure conduction case as well as the two convection cases, $\gamma_T = \pm 0.01$. The variation of the weld pool radius at the free surface (i.e. the half width of the pool) is shown in Fig. 14(b). The pool radius appears to be only a weak function of weld pool convection.

The results for the maximum temperature are shown in Fig. 15. In all cases, a rapid initial increase occurs due to the rapid growth in pool size which reduces the heat transfer into the weld pool by increasing the distance between the center of the free surface and the cooler melt front. As the pool grows larger the maximum temperature appears to approach a steady value near the evaporation limit, 2449°C. The results indicate evaporation is a major factor in determining the maximum temperature. Measurements of temperatures on the free surface of weld pools have been made by several investigators. Giedt *et al.* [29] used a pyrometer to measure the temperature at the center of a weld pool free surface immediately after turning off the arc. They estimated values between 1750 and 2000°C. Kraus [30] measured values between 1725 and 2525°C. The results obtained in this study strongly depend on the evaporation heat loss as determined from a thermodynamic model, which should probably be adjusted depending on the impurities being considered. The presence of impurities may be responsible for the wide range of results obtained from weld pool surface temperature measurements.

Figure 16 shows the process efficiency, defined as the ratio of the power entering the medium to the total arc power. (The total arc power is given by the product of the arc current and voltage. A radiation loss from the arc plasma results in only 90% of the arc power being incident on the surface.) For all cases the efficiency is initially high, near unity, but at 10 s it has decreased to 72% for $\gamma_T = 0.01$, 58% for $\gamma_T = -0.01$ and to 53% for pure conduction. These results are consistent with the measurements by Ghent *et al.* [31],

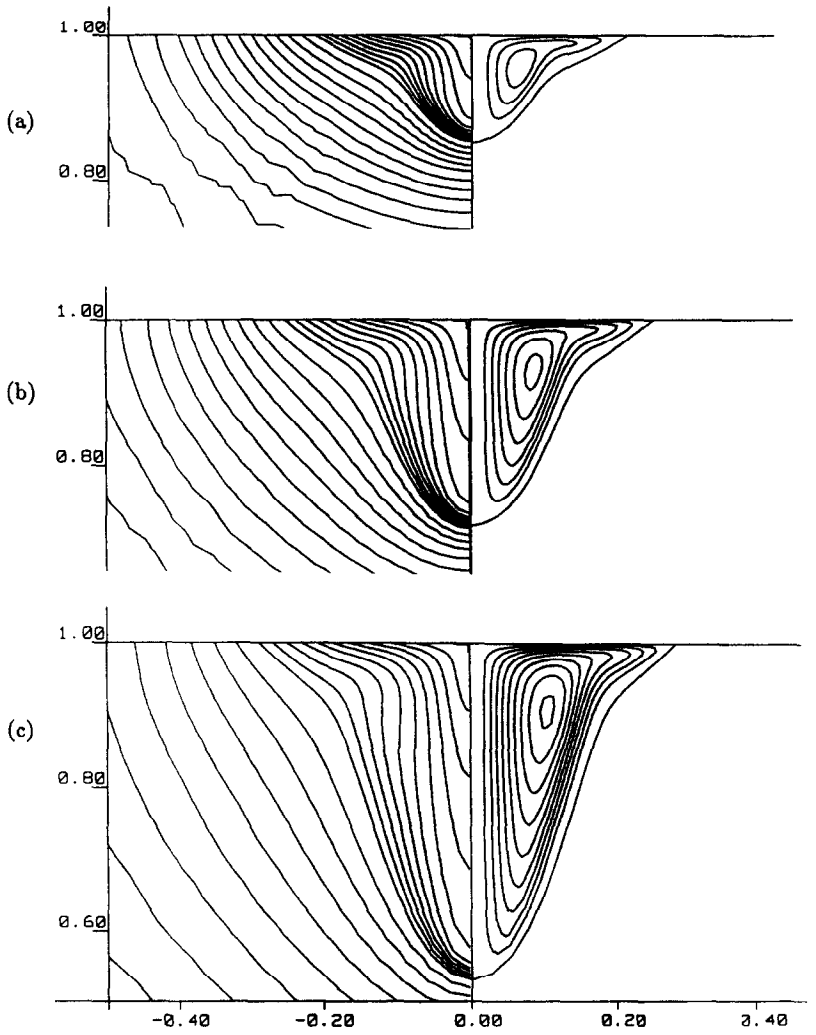

FIG. 10. The shape of the weld pool and the stream lines (right, shown in increments of 0.003 $cm^3\ s^{-1}$) and the temperature distribution (left, shown in 100°C contour intervals) in the vicinity of the pool for the $\gamma_T = +0.01$ dyne $cm^{-1}\ °C^{-1}$ case: (a) $t = 0.5$ s; (b) $t = 2$ s; (c) $t = 10$ s.

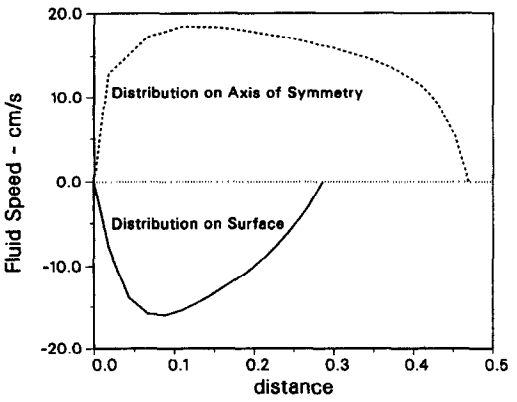

FIG. 11. The variation of the velocity (radial component) along the free surface and the velocity (axial component) along the axis of symmetry for the $\gamma_T = +0.01$ dyne $cm^{-1}\ °C^{-1}$ case.

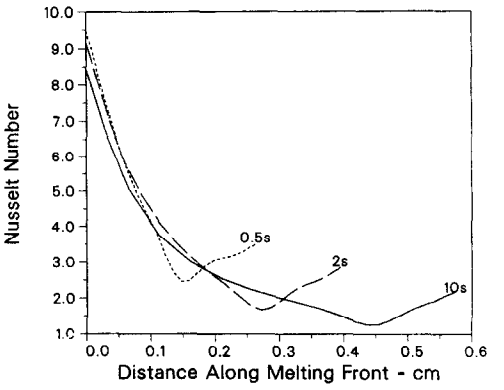

FIG. 12. The variation of the Nusselt number along the liquid side of the melt front for the $\gamma_T = +0.01$ dyne $cm^{-1}\ °C^{-1}$ case.

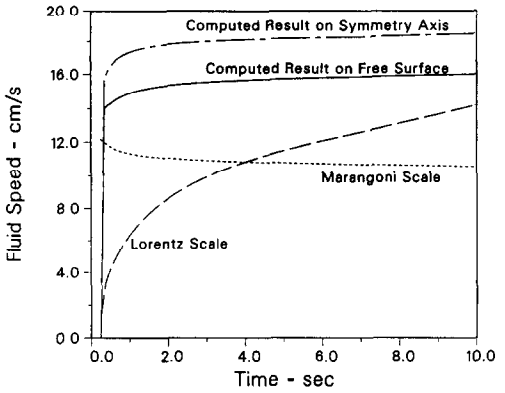

FIG. 13. The maximum fluid velocities on the free surface (radial component) and on the axis of symmetry (axial component) for the $\gamma_T = +0.01$ dyne cm^{-1} °C^{-1} case. The Marangoni and Lorentz velocity scales are shown for comparison.

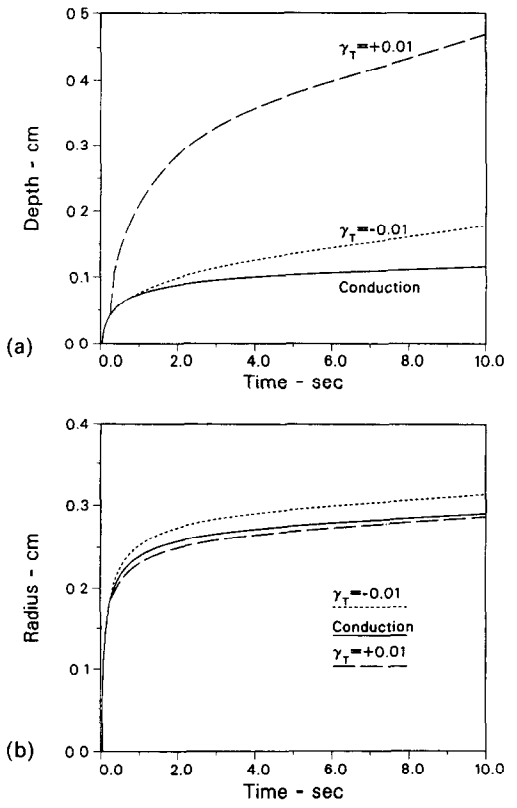

FIG. 14. The depth (a) and radius (b) of the weld pool as a function of time for pure conduction and for two convection cases, $\gamma_T = \pm 0.01$ dyne cm^{-1} °C^{-1}.

who reported efficiencies in the range of 60–80%. The results presented in Fig. 16 show that the effect of fluid motion is to reduce evaporation losses, regardless of the sign of γ_T.

6. SUMMARY AND CONCLUSIONS

The governing equations for unsteady axially symmetric conditions were solved to obtain the shape of the weld pool as a function of time. Included in the

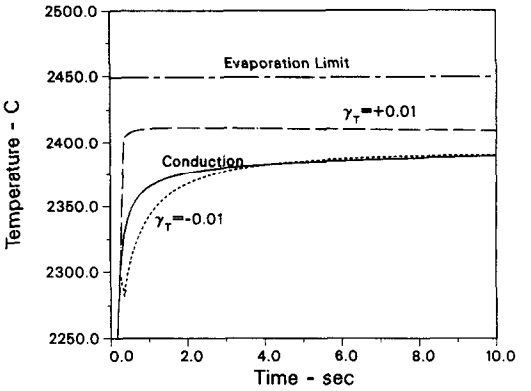

FIG. 15. The maximum temperature in the weld pool as a function of time for pure conduction and for two convection cases, $\gamma_T = \pm 0.01$ dyne cm^{-1} °C^{-1}.

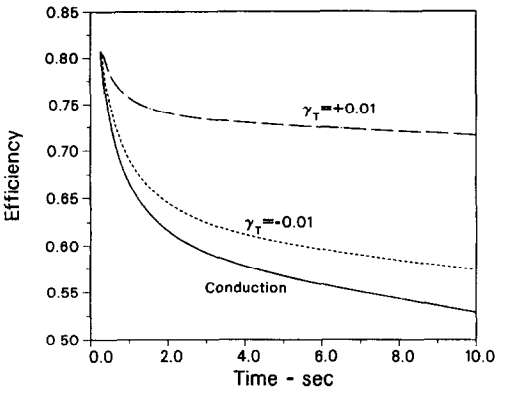

FIG. 16. The arc efficiency (defined as the ratio of the power entering the medium to the total arc power) as a function of time for pure conduction and for two convection cases, $\gamma_T = \pm 0.01$ dyne cm^{-1} °C^{-1}.

study were the effects of Marangoni forces, Lorentz forces, buoyancy, phase change and energy losses by evaporation and radiation. Maxwell's equations were solved to obtain the electric and magnetic fields. Calculations were made for three cases: pure conduction and convection with negative and positive γ_T. In all cases evaporation was a major energy loss mechanism which had a large effect on the maximum temperature. Convection decreased the evaporative energy losses and hence increased the size of the weld pool, regardless of the sign of γ_T. Convection significantly increased the depth of the weld pool but had only a small effect on the width.

The flow field for negative γ_T consisted of two vortices, one near the free surface of the pool driven by Marangoni forces and the other near the axis of symmetry driven by Lorentz forces. For this case, the Marangoni vortex convects heat to the outer perimeter of the pool which increases its width. The Lorentz vortex convects heat to the bottom of the pool which increases its depth. The flow field for positive γ_T consisted of a single, rapidly rotating vortex driven by both the Marangoni and Lorentz forces. This vortex convects heat to the bottom of the pool at a much

greater rate than does the Lorentz vortex for negative γ_T, which results in a much deeper pool.

The results for the maximum temperature in the weld pool approximately correlated with an energy balance between the maximum incident heat flux and evaporation. This indicated that a large amount of the energy incident at the center of the pool was lost by evaporation. The results for the efficiency were in the same range as published experimental data.

Acknowledgements—The authors are grateful to L. Bertram for his assistance in the formulation of the governing equations. The authors acknowledge K. Perrano [32] for his direct solver utility and J. Goldsmith [33] and V. Gabrielson [34] for their graphics utilities. This work was supported by the U.S. Department of Energy under contract No. DE-AC04-76DP00789.

REFERENCES

1. A. Block-Bolton and T. W. Eager, Metal vaporization from weld pools, *Metall. Trans.* **15B,** 461–469 (1984).
2. D. Rosenthal, The theory of moving sources of heat and its application to metal treatments, *ASME Trans.* **68,** 849–866 (1946).
3. R. L. Apps and D. R. Milner, Heat flow in argon arc welding, *Br. Welding J.* **2,** 475–485 (1955).
4. N. Christensen and V. Davies, Distribution of temperatures in arc welding, *Br. Welding J.* **12,** 54–75 (1965).
5. V. Pavlik, R. Tanbakuchi, D. A. Uyehara and P. Myers, Experiments and computed temperature histories in GTA welding of thin plates, *Weld J.* **48,** 295s–305s (1969).
6. E. Friedman and S. S. Glickstein, An investigation of the thermal response of stationary gas tungsten arc welds, *Weld J.* **55,** 408s–420s (1976).
7. G. S. Mills, Fundamental mechanisms of penetration in GTAW, *Weld J.* **58,** 21s–24s (1979).
8. D. R. Atthey, A mathematical model for fluid flow in a weld pool at high current, *J. Fluid Mech.* **98,** 787–801 (1980).
9. R. E. Craine and J. G. Andrews, The shape of the fusion boundary in an electromagnetically stirred weld pool. In *Metallurgical Applications of Magnetohydro-dynamics* (Edited by H. K. Moffatt and M. R. E. Proctor), pp. 301–313. The Metals Society, London (1982).
10. G. M. Oreper and J. Szekely, Heat- and fluid-flow phenomena in weld pools, *J. Fluid Mech.* **147,** 53–79 (1984).
11. G. M. Oreper and J. Szekely, A comprehensive representation of transient weld pool development in spot welding operations, *Metall. Trans.* **18A,** 1325–1332 (1987).
12. S. Kou and D. K. Sun, Fluid flow and weld penetration in stationary arc welds, *Metall. Trans.* **16A,** 202–213 (1985).
13. S. Kou and Y. H. Wang, Weld pool convection and its effect, *Weld J.* **65,** 63s–70s (1986).
14. C. Chan, J. Mazumder and M. M. Chen, A two-dimensional transient model for convection in laser melted pool, *Metall. Trans.* **15A,** 2175–2184 (1984).
15. Y. Fautrelle, Flow in the weld pool during TIG welding, *Soudage et Techniques Connexes* **39**(1–2), 12–19 (1985).
16. T. Zacharia, A. H. Eraslan and D. K. Aidun, Modeling of autogenous welding, *Weld J.* **67**(3), 53s–62s (1988).
17. N. Ramanan and S. A. Korpela, Fluid dynamics of a stationary weld pool, *The Winter Annual Meeting of the ASME*, Chicago (Edited by K. T. Yang). ASME (1988).
18. N. Tsai, Heat distribution and weld bead geometry in arc welding, Ph.D. Thesis, Massachusetts Institute of Technology (1983).
19. G. W. Sutton and A. Sherman, *Engineering Magnetohydrodynamics*. McGraw-Hill, New York (1965).
20. M. Choi, R. Greif and M. Salcudean, A study of the heat transfer during arc welding with applications to pure metals or alloys and low or high boiling temperature materials, *Numer. Heat Transfer* **11,** 477–489 (1987).
21. J. McKelliget and J. Szekely, Heat transfer and fluid flow in the welding arc, *Metall. Trans.* **17A,** 1139–1148 (1986).
22. D. Fan, M. Ushio and F. Matsuda, Numerical computation of arc pressure distribution, *Trans. Jap. Weld Res. Inst.* **15,** 1–5 (1986).
23. S. Ostrach, Low-gravity fluid flows, *Ann. Rev. Fluid Mech.* **14,** 313–345 (1982).
24. L. Leibowitz, Properties for LMFBR safety analysis, Argonne National Laboratories, ANL-CEN-RSD-76-1 (1976).
25. M. P. Kanouff, Numerical modeling of momentum and energy transport in a GTA weld pool using a moving, nonorthogonal grid, Ph.D. Thesis, University of California, Davis, California (1989).
26. S. I. Popel, B. V. Tsarevskiy, V. V. Pavlov and E. L. Furman, Combined influence of oxygen and sulphur on the surface tension of iron, *Russian Metall.* No. 4, 42–44 (1975).
27. V. Tszin-Tan, R. A. Karasev and A. M. Samarin, Surface tension of iron–manganese and iron–sulphur melts, *Russian Metall. Fuels* No. 2, 33–34 (1960).
28. C. R. Heiple and J. R. Roper, Effects of minor elements on GTAW fusion zone shape. In *Trends in Welding Research in the US* (Edited by S. A. David), pp. 489–520. Am. Soc. for Metals, Metals Park, Ohio (1982).
29. W. H. Giedt, X.-C. Wei and S.-R. Wei, Effect of surface convection on stationary GTA weld zone temperatures, *Weld J.* **63,** 376s–383s (1984).
30. H. G. Kraus, Experimental measurement of thin plate type 304 stainless steel weld pool surface temperatures, *68th American Welding Society Annual Meeting and 18th International AWS Brazing Conf.*, AWS, Miami, pp. 195–196 (1987).
31. H. W. Ghent, D. W. Roberts, C. E. Hermance, H. W. Kerr and A. B. Strong, Arc efficiency in TIG welds. *Arc Physics and Weld Pool Behavior*. The Welding Institute, London (1979).
32. K. J. Perrano, A general purpose simultaneous linear equation solver using skyline storage, Sandia National Laboratories, Livermore, California (1986).
33. J. E. M. Goldsmith, NEWPLOT 3: a general-purpose scientific plotting package, Sandia National Laboratories, Livermore, California (1985).
34. V. K. Gabrielson, GGP graphics processing using CRAY-ctss and VAX systems, Sandia National Laboratories, Livermore, California (1987).

DEVELOPPEMENT TEMPOREL DU BAIN FONDU GTA

Résumé—Les équations de transfert de la quantité de mouvement, de l'énergie et de l'électricité sont résolues numériquement pour obtenir le développement temporel d'un bain de soudure à arc de Tungstène (GTA) symétriquement axial. On inclut les effets de Marangoni, de Lorentz et des forces de flottement. La méthode des différences finies est utilisée pour les équations et la grille s'adapte à la forme et au déplacement du front de fusion. En général, la convection diminue les pertes d'énergie par évaporation sur le bain. Cela augmente la taille du bain fondu. La convection a un grand effet sur la profondeur du bain mais seulement un effet faible sur sa largeur. La force de Lorentz provoque des mouvements du fluide qui augmentent la profondeur du bain. Les effets de la force de Marangoni dépendent du signe du coefficient de température de la tension superficielle γ_T. Une valeur négative de γ_T provoque des mouvements du fluide qui suppriment les effets de la force de Lorentz et cela conduit à une profondeur convenable du bain. Une valeur positive de γ_T augmente les effets de la force de Lorentz et il en résulte un bain fondu très profond.

DIE INSTATIONÄRE AUSBILDUNG EINES GTA-SCHMELZBADES

Zusammenfassung—Die Erhaltungssätze für Impuls-, Energie- und Elektrizitätstransport werden numerisch gelöst, um die instationäre Ausbildung eines achsensymmetrischen Schmelzbades bei der Gas-Wolfram-Lichtbogenschweißung (GTA) zu ermitteln. Dabei werden die Einflüsse der Marangoni-, der Lorentz- und der Auftriebskräfte berücksichtigt. Die Gleichungen werden mit einem Finite-Differenzen-Verfahren gelöst, wobei das Gitter an die Form der Schmelzfront angepaßt wird und sich mit der Front bewegt. Im allgemeinen zeigt sich, daß die Konvektion den Energieverlust des Schmelzbades durch Verdampfung verkleinert, wodurch das Schmelzbad größer wird. Die Konvektion hat einen großen Einfluß auf die Tiefe des Schmelzbades, jedoch einen nur geringen Einfluß auf dessen Breite. Die Lorentz-Kraft bewirkt Fluidbewegungen, welche die Tiefe des Schmelzbades vergrößern. Die Auswirkungen der Marangoni-Kraft hängen vom Vorzeichen des Temperaturkoeffizienten der Oberflächenspannung γ_T ab. Ein negativer Wert von γ_T bewirkt Fluidbewegungen, welche den Einfluß der Lorentz-Kraft unterdrücken, und erzeugt ein völlig flaches Schmelzbad. Ein positiver Wert von γ_T bewirkt Fluidbewegungen, welche die Einflüsse der Lorentz-Kraft verstärken, was zu einem sehr tiefen Schmelzbad führt.

НЕСТАЦИОНАРНОЕ ПОВЕДЕНИЕ ОБЪЕМА РАСПЛАВА ПРИ ВОЛЬФРАМОВОЙ ДУГОВОЙ СВАРКЕ

Аннотация—С целью исследования нестационарного поведения осесимметричного объема расплава при вольфрамовой дуговой сварке численно решаются определяющие уравнения переноса импульса, энергии и электрического заряда. Учитываются эффекты Марангони, Лоренца и подъемных сил. Для решения уравнений используется конечно-разностный метод с сеткой, адаптированной к фотрме фронта расплава и движущейся вместе с ним в процессе плавления. Найдено, что конвекция снижает потери энергии в объеме расплава за счет испарения, что приводит к увеличению объема. Конвекция существенно влияет на глубину расплава и лишь незначительно – на его ширину. Сила Лоренца вызывает движение жидкости, которое увеличивает глубину расплава. Эффекты силы Марангони зависят от знака температурного коэффициента поверхностного натяжения γ_T. Отрицательное знажение γ_T вызывает движение жидкости, подавляющее эффекты силы Лоренца и приводящее к образованию довольно мелкого расплава. Положительное значение γ_T обусловливает движение жидкости, увеличивающее эффекты силы Лоренца и приводящее к образованию ожень глубокого расплава.